$Ca_3Ru_2O_7$: Interplay among degrees of freedom and the role of the exchange correlation

A. M León [1,2,3,*] J. W. González [4,†] and H. Rosner [2]

[1]*Departamento de Física, Facultad de Ciencias, Universidad de Chile, Casilla 653, Santiago, Chile*

[2]*Max Planck Institute for Chemical Physics of Solids, 01187 Dresden, Germany*

[3]*Facultad de Física, Pontificia Universidad Católica de Chile, Casilla Postal 306, Santiago, Chile*

[4]*Departamento de Física, Universidad Técnica Federico Santa María, Casilla Postal 110V, Valparaíso, Chile*

(Received 5 February 2023; revised 15 September 2023; accepted 7 December 2023; published 27 February 2024)

$Ca_3Ru_2O_7$ is a fascinating material that displays physical properties governed by spin-orbit interactions and structural distortions, showing a wide range of remarkable electronic phenomena. Here, we present a density-functional-based analysis of the interplay among degrees of freedom, such as magnetism, Coulomb repulsion (Hubbard U), and structural degrees of freedom, considering two exchange-correlation methods: local density approximation (LDA) and Perdew-Burke-Ernzerhof revised for solids (PBEsol). Our goal is twofold: first, to present a brief overview of the current state of the art on this compound underpinning to the last proposed theoretical models and experimental research, and second, to provide an alternative interpretation of the electronic properties compared with the previous theoretical models. Our findings show that $Ca_3Ru_2O_7$ displays several electronic states (metal, semimetal, and narrow insulator) as a function of Hubbard U while it exhibits structural transition depending on the functional. We disentangle the effect of the different degrees of freedom involved, clarifying the role of exchange correlation in the observed electronic and structural transitions.

DOI: 10.1103/PhysRevMaterials.8.024411

I. INTRODUCTION

Physics driven by spin-orbit interactions is among the most important topics in contemporary condensed matter physics [1,2]. Since the spin-orbit interaction is comparable to the on-site Coulomb repulsion and other relevant interactions, it creates a unique balance between competing interactions that drives complex behaviors and exotic states. In particular, compounds involving transition metals are technologically relevant. With their characteristic partially-filled d orbitals, they represent this nontrivial competition between interactions of different natures [3–5]. The series $Ca_{n+1}Ru_nO_{3n+1}$ compounds exemplify these characteristics; these $4d$-electrons systems present a perovskite structure, where the relative rotation and tilting of RuO_6 octahedra often affect the electronic properties depending on the number of layers (n in $Ca_{n+1}Ru_nO_{3n+1}$). Among these, the $Ca_3Ru_2O_7$ compound (CRO) presents several quantum phenomena such as electronic phase transitions, colossal magneto-resistance, spin density waves, or quantum oscillations [6–9]. Early works suggested that CRO is a hallmark material exhibiting both metallic and insulator states. Due to these characteristics, CRO is cataloged as a peculiar material [10] whose further comprehension could provide new routes to understand the complex interplay among spin, orbital, charge, and lattice degrees of freedom present in $4d$ oxides [11,12].

Currently, CRO is recognized as a polar metal holding a strong interplay between spin-orbit coupling (SOC) and structural inversion symmetry [11,13], which leads to their exotic properties. Recent experimental results have given new perspectives to manipulate and continue exploring their quantum states. In this context, metamagnetic phases have been observed [14], which may host mixed textures similar to the chiral magnetic skyrmions. Thus it constitutes an ideal playground to study diverse antiferromagnetic-ferromagnetic states near metamagnetic transitions. Also, polar domain formation was found in CRO, which may be controlled by ferroelectric switching. This last discovery opens new exciting questions about the mechanism behind that support such domains in polar metals [15]. Moreover, it was shown that CRO exhibits extraordinary lattice flexibility since its electronic states can be tuned by manipulating their crystalline axes via external magnetic fields and under pressure [7,16]. The studies mentioned above open a new research stage on the CRO system. The appearance of magnetic textures, polar domains, and the possibility of manipulating electronic states by lattice deformation could give novel perspectives to search for the next generation of ferroelectric compounds with novel functionalities [17].

The CRO structure is defined by RuO_6 planes intercalated with calcium atoms. Due to the strong spin-orbit coupling present in the Ru atoms, noncollinear magnetism is expected [18,19]. The relative tilts and rotations of the RuO_6 octahedra generate a noncentrosymmetric pattern that determines the

*andrea.leon@uchile.cl

†jhon.gonzalez@usm.cl

interaction between Ru planes in these perovskite-like structures. In particular, one of the most striking characteristics of CRO is its phase transitions under temperature, exhibiting a first magnetic transition at the Néel temperature of 56 K (T_N). This first transition is associated with the spins aligning ferromagnetically within each bilayer in the [100] direction but antiferromagnetically coupled between bilayers (AFM-*a*). A second structural and magnetic transition happens at 48 K (T_S), where a *c*-axis lattice parameter compression occurs and the spins are reoriented from the [100] to the [010] directions (AFM-*b*) [6,8,20].

Below T_S, the in-plane resistivity starts to increase with cooling, showing a local maximum at $T \approx 30$ K. In early work [6], the phase transition at T_s was discussed as a metal-insulator transition, and the temperature region between 30 K and T_S was described as an insulating phase of $Ca_3Ru_2O_7$. The nature of these phases (either metallic or insulator) has been controversial in the literature [12]. In this context, it was suggested that different growth batches of $Ca_3Ru_2O_7$ crystals yield distinct low-temperature properties, ranging all the way from the metallic ground states [8,9,21,22] to insulating phases [6,23,24]. The divergent experimental observations have motivated an intense research and debates for more than one decade [6–9,21–24].

Using a theoretical approach based on the density functional theory (DFT), we explore the electronic and magnetic properties of CRO crystals to verify the conditions that lead to either metallic or nonmetallic ground state solutions. Here, we study the interplay among Coulomb repulsion (Hubbard U), spin-orbit coupling (SOC), structural degrees of freedom (positions and volume), and exchange correlation. We compare our results against the latest experimental and theoretical results on CRO. Furthermore, we contrast the electronic band structure of CRO using two exchange correlations: PBEsol (PS) and LDA approximations, and we perform a linear response approximation calculation implemented by Cococcioni-Gironcoli [25]. We establish the upper and lower limits of the optimal Hubbard U values. The contrast of our results against the experimental evidence reveals that LDA + U ($0.2 \leqslant U \leqslant 2.0$ eV) models properly the electronic and structural properties of CRO.

II. THEORETICAL ADVANCES

One of the biggest problems is to conciliate the metallic or insulator nature of the phase between $30 \lessapprox T < T_S$, in which some experimental works suggest a metal/semimetal behavior [8,9,21,22] and others an insulator phase [6,23,24]. From a theoretical point of view, early DFT studies have reported electronic properties under different approximations. Collinear calculations predict AFM ground state with an FM and AFM spin coupling intra- and interlayer [26], respectively, in agreement with the experimental report [20]. Along with the FM configuration, it was found that the system exhibits a nearly half-metallic state. Later, noncollinear calculations explored the role of U and SOC on the electronic properties, indicating the U region in which the system could be metallic or insulator, which in turn depends on the magnetic moment orientation [27].

Recent experimental and theoretical studies have given new perspectives about the nature of CRO below T_S, reaching a better agreement between theory and experiments. It was revealed that CRO does not have a real insulator phase. A pseudogap behavior around Γ point appears and several bands cross the Fermi level [11,13]. Despite this advance, the mechanism that causes the phase transitions around T_S is still controversial. On the one hand, it is proposed a Lifshitz-like transition at T_s together with a new structural transition at $T \approx 30$ K, as a result of the RuO_6 octahedral distortions and hybridization changes induced by the enhancement of the Coulomb interactions upon cooling [28]. On the other hand, it was suggested that the phase transition at T_s arises due to the thermal population reduction, opening a gap at the Fermi level [11]. These hybridization changes induce an electronic energy gain favoring the spin reorientation through Rashba-type spin-orbit coupling, accompanied by structural changes simultaneously [11]. Previous theoretical works have discussed the role of fundamental interactions such as Coulomb and spin-orbit coupling considering GGA [27,28] and PS [28] approximations. However, in this work, we aim to gain insight into the interplay among several degrees of freedom, such as magnetism, SOC, Hubbard U repulsion, and structural degrees of freedom, considering the role of the exchange correlation (LDA and PS) in the electronic and structural properties of CRO.

Why is it so complicated to understand the electronic structure of CRO? From a theoretical point of view, studies based on DFT have observed that the unconventional magnetic and electronic properties are dictated by the competition of multiple degrees of freedom (charge, spin, SOC, lattice). This makes the electronic states highly sensitive to the electronic interactions and correlations. Early studies using GGA approximation demonstrate a metallic state and highly anisotropic behavior of CRO. They suggested for the first time the crucial role of spin-orbit interaction, whereas a metal-insulator transition happens by the interplay of SOC and Coulomb repulsion (U) (for $U > 3$ eV) [27]. Later, other studies considering spin-orbit interaction with LDA and GGA showed that the system has a semimetal state. Here, it was evinced that GGA fails to describe the band structure at Γ point through comparison with ARPES spectra [11]. Finally, recent works performed studies using GGA along with PS approximation, considering the interplay among SOC + U + structural degrees of freedom. This study revealed that for small U values, it is possible to control the band occupation around the Fermi level, giving a good agreement with the ARPES spectra for $U \geqslant 1.4$ [28]. However, it is necessary to propose a new structural phase transition which is not reported by experiments so far.

III. CALCULATION DETAILS

We perform a theoretical analysis using the density functional theory with spin-orbit coupling (SOC). We use the plane wave pseudopotential method implemented in the Vienna *ab initio* simulation package (VASP) [29] within the PBEsol functional (PS) [30] and the local density approximations (LDA) [31]. PS belongs to generalized gradient approximations (GGA), and it gives structural properties

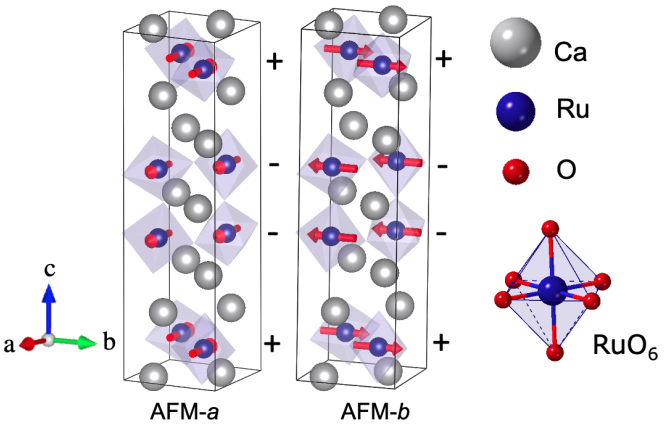

FIG. 1. $Ca_3Ru_2O_7$ in two antiferromagnetic phases, AFM-*a* and AFM-*b*, with ferromagnetic coupling within the layers and antiferromagnetic coupling between the bilayers. The $+/-$ signs represent the relative orientation of the Ru in-plane magnetic moments: "+" for magnetic moments oriented in the axis direction and "−" for those oriented in the opposite direction.

closer to the experimental values when compared to the results of PBE [32]. The electronic valence considered are the following: Ru: $5s^1 4d^7$ and O: $2s^2 2p^4$ (for LDA and PS), and Ca: $3s3p4s$/Ca: $2sp^6 s^2 d^{0.01}$, for PS/LDA, respectively. We use a plane wave energy cutoff of 650 eV and set a Regular Monkhorst-Pack grid of $5 \times 5 \times 3$ to perform the atomic relaxation and $7 \times 7 \times 5$ to perform the self-consistent calculation. We use a fine *k*-grid $14 \times 14 \times 5$ within the tetrahedron method for the density of states. We perform the structural optimization of the unit cell until a force convergence threshold of at least 10^{-3} eV/Å per atom.

To consider the electronic correlation effects in *d* orbitals of Ru atoms, we consider a range of Hubbard on-site Coulomb parameters through the Dudarev approximation [33]. Also, we employ the Liechtenstein scheme for comparison propose [34]. Later, we employ the linear response to estimate the optimal Hubbard *U*; we follow the linear approach method [25]. The linear response was computed by introducing the interacting and noninteracting occupation response with respect to the localized perturbations up to $V = \pm 0.2$ eV in the Ru atoms; we compare the Ru *d*-orbital occupation upon the perturbation *V* along LDA/PS, and with/without SOC.

IV. RESULTS AND DISCUSSION

CRO crystallizes in an orthorhombic structure with space group [20] $Bb2_1m$ (a full description of the structure is available in Ref. [35]). The atomic positions are taken from the neutron diffraction measurements [20] at 8 K. To reproduce the different collinear AFM configurations, the unit cell includes 48 atoms; there are 12 Ca atoms, 8 Ru atoms, and 28 O atoms. Figure 1 shows the lattice structure of CRO, with two possible magnetic configurations experimentally reported at $T < 48$ K and $T > 56$ K called AFM-*b* and AFM-*a*, respectively. The $\pm\mathbf{a}$ and $\pm\mathbf{b}$ notation means the ferromagnetic states with the direction in which the in-plane magnetic moments align. We also introduce the FM-*b* configuration, which means an FM coupling between layers with the magnetic moment aligned along the *b* direction.

TABLE I. Magnetic configuration (conf.) ground state, *m* the magnetic moment per Ru-atom, V(RuO_6) is the RuO_6 octahedral volume (Å^3), and *l*(Ru-O) is the Ru-O bond average length (Å) for the most stable magnetic configuration considering $U = 0$ eV. The third-row label as "Exp" corresponds to the experimental data [20].

Appr.	Magnetic conf.	m (μ_B)	V(RuO_6) (Å^3)	*l*(Ru-O) (Å)
LDA	FM-*b*	0.83	10.53	1.992
PS	AFM-*b*	1.36	10.54	1.993
Exp. [20]	AFM-*b*	1.8	10.53	1.992

1. Exchange correlation effects, U = 0 eV.

In the PS approximation, the ground state presents an AFM-*b* configuration with a magnetic moment (*m*) of 1.36 μ_B (calculated in a Wigner-Seitz (WZ) radius 1.323 Å). The energy difference between the AFM-*b* and AFM-*a* configuration is 0.88 meV/Ru ($E_{\mathrm{AFM}-a} - E_{\mathrm{AFM}-b}$). Within the same approximation, the FM-b phase presents a total magnetic moment of 1.92 μ_B; this value overestimates *m* about a 6% concerning the *m* measured by previous experimental reports [20]. The energy differences between the AFM-*b* state and FM-*b* phase is 1.69 meV/Ru ($E_{\mathrm{FM}-b} - E_{\mathrm{AFM}-b}$).

In contrast, the LDA approximation reveals an FM-*b* ground state with a low total magnetic moment of 0.83 μ_B. This state is more stable than AFM-*b* and AFM-*a* configuration with an energy difference of −5.85 meV/Ru ($E_{\mathrm{FM}-b} - E_{\mathrm{AFM}-b}$) and −2.35 meV/Ru ($E_{\mathrm{FM}-b} - E_{\mathrm{AFM}-a}$), respectively. Besides, the AFM-*a* phase has lower energy than the AFM-*b* phase by −2.67 meV/Ru. Despite the mismatch in the magnetic stability order between PS and LDA, both approximations reproduce the experimental crystal structure [20] (see Table I, calculation at the experimental volume 580.04 Å^3, considering positions degrees of freedom).

Going further, we perform a volume cell relaxation; these values are reported in Table S1, and our results for the most stable phase are shown in Table S2, Ref. [36]. We can see that under volume relaxation the most stable magnetic ground state does not change.

2. Electron-electron correlation effects

Now, we will study the effect of electron-electron repulsion on the electronic and structural properties considering positions degrees of freedom. Based on previous works [28], we use Hubbard *U* values in the [0, 2] eV range and considering the volume given by the experimental reports [20]. Figure 2 shows the effect within the PS and LDA approximations of the Hubbard *U* interaction for the magnetic anisotropy $\Delta E = E_a - E_b$ ($E_a = E_{\mathrm{AFM}-a}$ and $E_b = E_{\mathrm{AFM}-b}$), the magnetic moment per Ru atom *m*, and RuO_6 octahedra volume (V-RuO_6).

On the one hand, we will start with the LDA analysis, represented with red dots in Fig. 2. The magnetic anisotropy as a function of the Hubbard *U* is presented in Fig. 2(a). When the Hubbard *U* interaction is included, the AFM-*b* ground

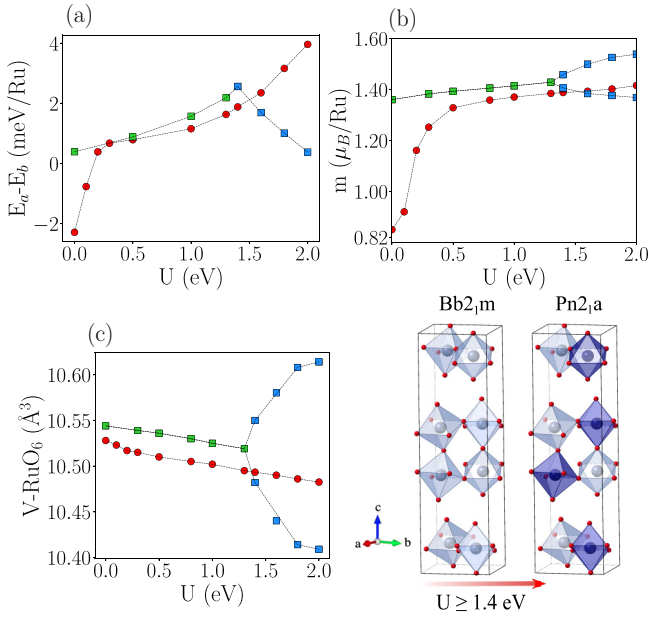

FIG. 2. Effect of electron-electron repulsion (Hubbard U) on the physical properties of CRO. In (a), magnetic anisotropy $E_a - E_b$, (b) magnetic moment per Ru atom [measured in the Wigner-Seitz radius (1.323 Å)], and (c) volume of RuO_6 octahedra as U increases from 0 to 2.0 eV. Red and green dots correspond to the crystal phase $Bb2_1m$ with LDA and PS approximation, respectively, and blue dots correspond to the $Pn2_1a$ structure with PS approximation. Note in (b) and (c) for $U \geqslant 1.4$ eV and PS approximation, the Ru atoms in the $Pn2_1a$ phase present two different crystallographic environments and thus two different magnetic moments and volumes. The bottom right panel displays the structural change from $Bb2_1m$ to $Pn2_1a$ for $U \geqslant 1.4$ eV; the different octahedra color on the $Pn2_1a$ structure symbolizes the different environments in this cell.

state is restored for $U \geqslant 0.2$ eV (this configuration became more stable as $\Delta E > 0$). In Fig. 2(b), as expected, we observe that the U term increases the magnetic moment rise, from $m = 0.84\ \mu_B$ at $U = 0$ to $m = 1.16\ \mu_B$ at $U = 0.2$ eV, then the magnetic moment increases monotonously to $U = 2.0$ eV. Finally, in Fig. 2(c), we found that the octahedra volume decreases as the U term increases.

On the other hand, for the PS approximation represented with blue and green dots in Fig. 2, we can observe a non-monotonous behavior as the U term increases. Here, we identify the critical U term of $U_c = 1.4$ eV. When U increases above the U_c, a spontaneous structural transition appears, changing from $Bb2_1m$ to $Pn2_1a$ structure (depicted in the bottom-right panel). This transition could be associated with the interplay of the SOC + U and structural degrees of freedom [28]. In panel (a), after U_c we note a drop in the anisotropy value, where for $U = 2$ eV, we recover the value obtained for $U = 0$. In panel (b), the magnetic moment after U_c shows two different values associated with the two crystallographic environments observed (see Fig. 2 bottom-right panel). A similar behavior appears when we look at the volume of the RuO_6 octahedron in panel (c). Additionally, we have verified that the spontaneous structural symmetry change is independent of the structural degrees of freedom; further comments are in Sec. I of Ref. [36].

To properly describe the AFM-b ground state within the LDA approach, it is necessary to consider a large Hubbard U ($U \geqslant 0.2$ eV). For $U < 0.2$ eV, the most stable system is the AFM-a configuration [see Fig. 2(a)]. Furthermore, comparing Figs. 2(a) and 2(b), we can identify that the regions with AFM-a as the ground state, $E_a - E_b < 0$, the magnetic moment is smaller, $m < 1.0\ \mu_B$. In the regions with AFM-b as the ground state, $E_a - E_b > 0$, the magnetic moment is larger than $1\ \mu_B$. Since the LDA approximation does not reproduce the experimental magnetization of the ground state for smaller U values ($U < 0.2$ eV), to discuss the theoretical results with the experimental data, we compare the band structure within PS and LDA approximations considering $U_{PS} = 0$ and $U_{LDA} = 0.5$ eV, respectively.

We should note that the magnetic moment observed for PS and LDA is lower than the magnetic moment experimentally reported (see Table I). This is because the plane wave approximation yields minor uncertainties in predicting localized quantities, like the magnetic moment and the charge per atomic site. The m displayed in Fig. 2(b) is measured in the WS radius, then lower than the total magnetic moment. In order to compare our m results with the magnetic moment reported by the experiment for the AFM-b phase ($m \sim 1.8\ \mu_B$) [20], we compute an FM-b configuration by completeness in order to obtain the total magnetic moment by Ru atom as a U function for both approximations; see details in Ref. [36] (see Fig. S2).

The band structure and its projection in atomic orbitals for the PS and LDA approximations are shown in Fig. 3. We will compare systems with similar magnetic anisotropy and magnetic moments [see Figs. 2(a) and 2(b)]; for the PS approximation, we will take a value $U = 0$ eV, and for the LDA approximation, we choose a U = 0.5 eV. In Fig. 3, we can see that the band structure and its projection are very similar, independent of the approximation used. The system exhibits a metallic character with subtle differences at the Fermi level for both approximations, mainly around the Γ point. The valence band is mainly composed of the contribution of atoms of Ru and O (see Fig. S3). The Ru ions are embedded in an octahedral environment formed by the oxygen atoms; the octahedral crystal field splits the Ru 4d atomic levels, raising the e_g and decreasing the t_{2g} orbitals. This configuration yields a low-spin state, with the four 4d electrons partially filling the three t_{2g} orbitals, leaving two unpaired electrons per Ru atom [35] aligned as seen in the right panel of Fig. 3 and in the partial density of states displayed in Ref. [36] (see Fig. S3). The orbital projection is considered with octahedra aligned to the unit cell; thus, in this reference, the t_{2g} and e_g orbitals correspond to (d_{xy}, d_{xz}, d_{yz}) and ($d_{x^2-y^2}$, d_{z^2}), respectively.

In the case of PS, we can note a metallic character at Γ; however, this is not observed in the LDA approximation. We observe a local band gap of 65 meV around the Γ point in the LDA approximation. For both approximations, we identify a Dirac-like behavior at M_x, in agreement with the ARPES measurements [11]. Along M_x-X path, a small band crossing around the Fermi level is found. The projected band structure around the Fermi level reveals a dominant contribution

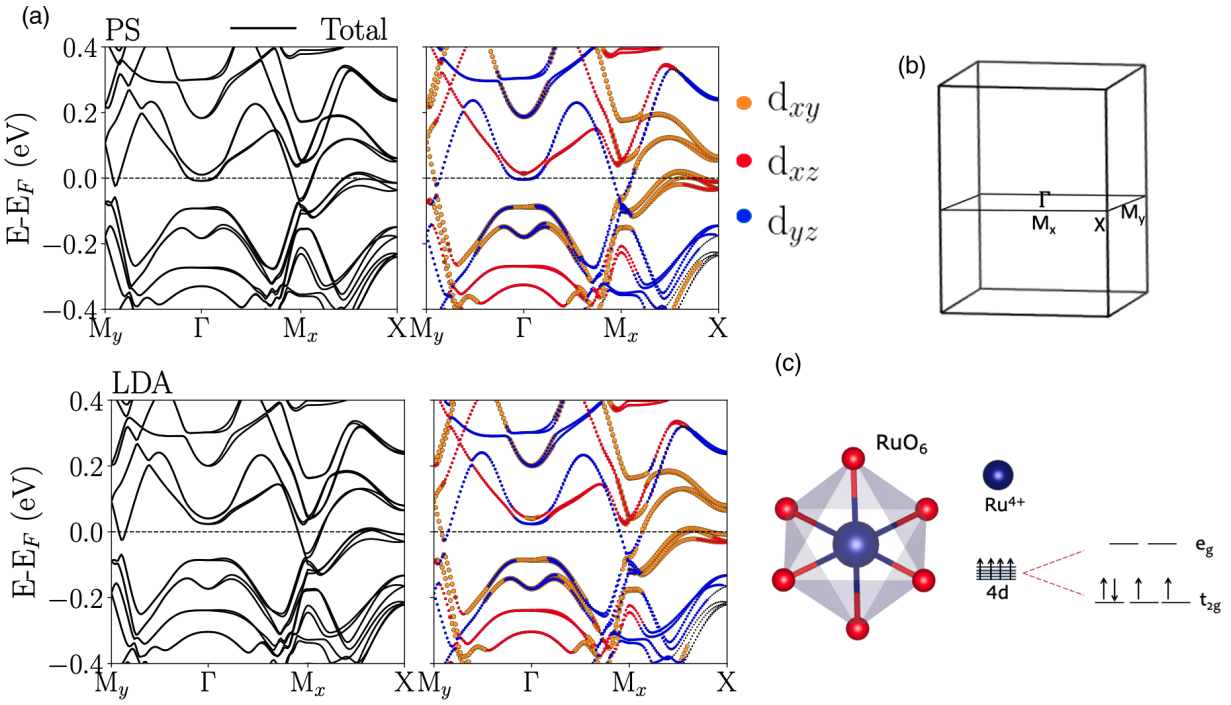

FIG. 3. (a) The upper and lower panels show the band structure along PS and LDA calculations, respectively, for U = 0 and 0.5 eV in each case. (Right) Total bands and the decomposed orbital bands, in which the orbitals have a 25%–75% of occupation per orbital. (b) Surface Brillouin zone of $Bb2_1m$ structure. (c) Diagram of the crystal field splitting of the Ru 4d states in the octahedral environment. The orbital projection is considered with octahedra aligned to the unit cell; thus, in this reference, the t_{2g} and e_g orbitals correspond to (d_{xy}, d_{xz}, d_{yz}) and ($d_{x^2-y^2}$, d_{z^2}), respectively.

(between a 25% to 75% per orbital) of the d_{xy}, d_{xz}, and d_{yz}. The $d_{x^2-y^2}$, d_{z^2} orbitals represent less than 25% of the projection, and therefore they are not displayed. In both projections, we can see that around the Γ, the dominant states belong to the hybridization between d_{xy}-d_{yz} (below the Fermi level) and d_{yz}-d_{xz} without hybridization (above of Fermi level). Along M_y-Γ the bands are mainly composed of d_{xy} and d_{yz} orbitals. The Dirac-like bands are characterized by d_{xy}, d_{yz} orbitals, and finally, along M_x-X path, the most dominant contribution came from d_{xy} and d_{xz} states (around the Fermi level).

In the case of LDA for $U = 0$, a different trend is found on the band dispersion as well as for AFM-a (ground state) and AFM-b configuration. Here, we evinced a metallic behavior along all the high symmetry points (details in Ref. [36], Fig. S4).

We systematically study the effect of Hubbard U repulsion on the band structure; in Fig. 4, we show the evolution of the band structure for PS and LDA approximations as U term changes in a range from 0.5 to 2.0 eV. In general, for the same U term value, there are similarities between PS and LDA; below the Fermi level, the bands around the Γ point that are mainly composed by d_{yz} and d_{xy} orbitals, these orbitals are pushed to lower energies as the U term increases, favoring the hybridization between these orbitals (see Ref. [36], Fig. S5). Along M_x to X path, we can observe that these states are slightly pushed below the Fermi level. These bands are rather modified because they are mainly composed of d_{xy} orbitals being close to integer filling and then exhibiting a less grade of hybridization (see Fig. 3 right panel). Besides, from M_y-Γ as the Hubbard U increases, the bands are pushed to higher energies inducing a band distribution aiding the occupation of the d_{xz} orbitals, which slightly hybridize with the d_{xy} orbitals just below the Fermi level (see Ref. [36], Fig. S5). Although, for PS approximation, we can distinguish three ranges of U-term values. The first region, between $0 \leqslant U \leqslant 1.4$ eV, is characterized by a metallic state (with a band crossing the Fermi level at Γ, in the first three plots of the top panel in Fig. 4). In the second region, for $1.4 \leqslant U \leqslant 1.8$ eV, we can observe that the bands at Γ and the Dirac-like bands are pushed to high energies given to the system a semimetallic character (due to the gap around Γ point). These changes are simultaneous with the phase transition when symmetry changes from $Bb2_1m$ to $Pn2_1a$, as discussed before [28].

When examining the band structure along the LDA approximation (lower panels of Fig. 4), unlike in the PS case for lower U values ($U < 1.4$ eV), we do not observe bands crossing the Fermi level in the vicinity of the Γ point and the $Bb2_1m$ structure continues to be the most stable configuration. Although, as in the case of PS, we can observe that for $U \geqslant 1.4$ eV, it favors a semimetallic state in which the Dirac-like bands (at M_x) are pushed to higher energies, besides the bands get closer to the Fermi level near the M_y for $U \geqslant 1.8$ eV.

3. *Effects of the functional and structural degrees of freedom*

To determine the mechanism promoting the electronic and structural changes under PS approximation, we perform an

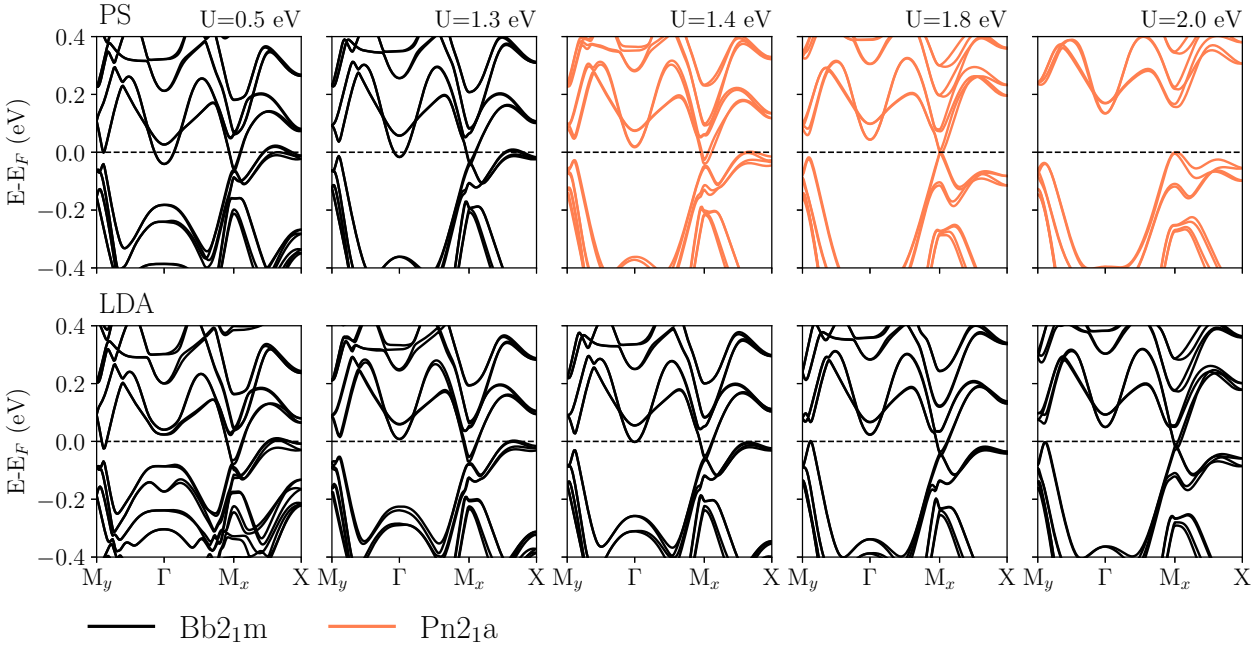

FIG. 4. The upper and lower panels display the band structure computed with PS and LDA approximation, respectively. The black band corresponds to the $Bb2_1m$ structure and the color band to the $Pn2_1a$ phase. Calculation considering SOC + U+ position degrees of freedom.

additional calculation to distinguish the effects of the functional choice and the structural phase in the electronic band structure. For this sake, first, we take the structure obtained with PS for $U \geqslant 1.4$ eV ($Pn2_1a$ phase), and with a frozen geometry, we calculate the electronic bands within the LDA approximation. In Fig. 5, we compare the band structure for PS and LDA, keeping the geometry of the PS approximation ($Pn2_1a$). In the left panel of Fig. 5, we show the band structure for $U = 1.8$ eV, the system with $Pn2_1a$ (PS approximation) remains with a semimetal state. Instead, we can observe that the Dirac-like bands are suppressed under LDA approximation, emerging a band gap of around M_x-point. Furthermore, for $U = 2.0$ eV, shown in the right panel of Fig. 5, both approximations show a narrow bandgap insulator character with

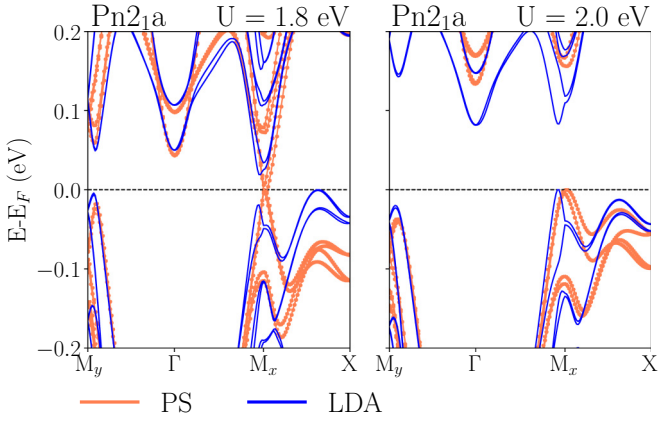

FIG. 5. Band structure for $Pn2_1a$ structure performed with PS (orange bands) and LDA (blue bands) approximations with $U = 1.8$ (left) and 2.0 eV (right).

a gap at M_x of 0.08 eV for LDA and 0.18 eV for PS approximation. Secondly, to reveal the effect of the structural degrees of freedom in the band structure for the $Bb2_1m$ phase, we have calculated this without and with structural degrees of freedom along with PS and LDA approximation. In the first case, we find that the main role of Hubbard U interaction is to control the band occupation around the Fermi level, favoring the gap increases around Γ and the emergence of hole-like bands close to M_y (for U > 1.4) while changing the Hubbard U from 0 to 2 eV (see Ref. [36], Fig. S8). In the second case, the changes in the lattice vectors induce slight modifications of the bands around the Fermi level, affecting mainly the gap at Γ (see Ref. [36], Fig. S10 and S11). In particular, the metallic character is still present for $U = 1.4$ eV within the PS approach; thus, the structural transition is not concurrent with the electronic transition from metal to semimetal (gap at Γ point).

4. Comparison with experimental evidence

In this section, we aim to get into contact with the experiments; therefore, we focus on which approximation and parameters best describe the band structure and magnetic configuration (AFM-*b*) experimentally measured in CRO samples. As discussed in Sec. II, understanding physical properties has been a significant challenge. There are inconsistencies between different experimental measurements and theoretical predictions. One of the main inconsistencies between observations and theory was that band structure calculation performed by DFT calculations predicted that CRO is a semi-metal with a high carrier concentration [9]. However, on the one hand, single-crystal measurements characterized CRO as a low carrier-concentration material on the verge of a metal-insulator. On the other hand, the ARPES measurements reveal that CRO displays a low-carrier metallicity but is char-

acterized by a semimetallic state with a gapped Fermi surface [11,13]. A summary of contradictions around CRO can be found in Ref. [12].

A previous theoretical study (Ref. [28]) proposed a mechanism to model the band structure and Fermi surface of CRO at low temperatures based on DFT calculations (along with PS approximation). The suggested mechanism aim to explain the electronic changes between $T_S < T < 30$ K, taking into account Hubbard U in the range $0.5 < U < 1.6$ eV, in which at $U = 1.4$ eV emerges a gap at Γ point, accompanied of a spontaneous structural transition from the $Bb2_1m$ to $Pn2_1a$ structure. In such a scenario, the emergence of the semimetallic state could be related to the gap seen below 45 K in the optical conductivity spectra [22]. Besides, the broken translational symmetry of the $Pn2_1a$ structure could allow the charge (spin) density wave transition agreeing with some experimental proofs [9].

However, recently a series of independent experiments have successfully reconstructed the Fermi surface of CRO [11–13], offering a novel approach to understanding the evolution of the electronic structure as the temperature decreases. The experimental evidence shows that CRO presents a semimetallic character at low temperatures [11,13], in which the band structure displays a gap around Γ point, Dirac-like bands at M_x, and bands intersecting the Fermi level near the M_y. Each work [11,13] reveals a key aspect to consider identifying the mechanism underneath the CRO phase transition. On the one hand, it was shown that the reconstruction of the Fermi surface is incompatible with the translational symmetry-breaking density waves [13]. On the other hand, a band gap magnitude of ∼10 to 15 meV around the Γ point was estimated, comparable to the pseudogap observed in optical spectroscopy spectra [11]. These observations bring us several constraints to impose on our calculations.

After a systematic study and comparison with the most recent experiments, our results indicate that the LDA + U approximation is the one that most accurately represents the complex behavior exhibited by CRO. The LDA + U approximation successfully identifies the magnetic ground state (AFM-b configuration) and the occupation bands in agreement with the recent experimental reports [13].

The subtlest region is to model the band spectrum along the high symmetry lines, specifically near the Γ and the M_y; this region is quite sensitive to U value; however, these regions are key, as we explained before the experiment evidences a pseudogap (around Γ) and hole pocket (near the M_y) and Dirac-like bands (at M_x) [13], given a semimetallic character to the system. In contrast to the PS approach, LDA can modulate the band occupation at Γ point in the studied range of U values. For instance, the LDA + U with $U = 0.5$ eV evidences a band gap of 96 meV at Γ; this value is in the same order as ARPES measurements [11]. Besides, the bands are getting closer to M_y for $U \geqslant 1.8$ eV; however, for this range of U, the band dispersion around Γ is pushed down to lower energies, increasing the size gap. Additionally, we have identified that the main band contribution around the Fermi level comes from d_{xy}, d_{xz} and d_{yz} orbitals in which d_{xy} does not cross the Fermi level for $U > 0.5$ eV (see Fig. S5) in agreement with the experimental reports [13]. In the case of PS, several issues are found as U increases: Below $U < 1.4$ eV band crosses the Fermi level at Γ point and above $U \geqslant 1.4$ eV due to a spontaneous transition toward the $Pn2_1a$ structure, being this structural phase reported theoretically until now [28] in the best of our knowledge.

In order to dig into the role of the Hubbard U approximation and how the double counting, as well as the directional dependence, can affect the observed results, we performed the same calculations using the Liechtenstein approximation [34] (along PS). A detailed analysis is provided in Sec. III of the Ref. [36]; here, we summarize the main findings. We have observed that for $U < 1.4$ eV Dudarev and Liechtenstein approximations have the same trend. However, at $U \geqslant 1.4$ eV, using Dudarev lead to the spontaneous phase transition and with Liechtenstein, the $Bb2_1m$ phase stays stable. With this last approximation, the transition happens for $U \geqslant 2.0$ eV, emerging a narrow insulator phase.

What is the underlying mechanism for the observed structural transition when considering the PS approximation with spin-orbit coupling (SOC) and Hubbard U repulsion effects?

The spontaneous transition appears independent of the Hubbard U approximation. To inspect the role of SOC we have performed calculations considering Hubbard U and structural degrees of freedom without SOC. We find that without SOC, the spontaneous structural transition does not appear. Our calculations show that $Bb2_1m$ is stable considering positions and volume degrees of freedom. However, the phase $Pn2_1a$ is unstable, making it difficult to achieve an accurate convergence. These results disagree with the studies reported in Ref. [28].

When spin-orbit coupling effects are considered, the direction of magnetization changes from point to point, inducing a complex magnetic landscape. The PBEsol approximation belonging to the family of generalized gradient functional approximations (GGA) is more susceptible to convergence problems and can cause symmetry changes to stabilize the system [37].

5. Linear response determination of U term

Going one step further, we employ a perturbative approach to determine a value for the Hubbard U interaction. However, this method tends to overestimate the value of U. Note that the DFT + U approach also has limitations and should be considered a pragmatic way to partially eliminate the self-interaction errors inherent in DFT. In addition, the effective U-value depends on several factors that limit their transferability, such as atomic coordination and calculation parameters [38,39] (pseudopotentials, basis-set). We compute the Hubbard U term through a constrained DFT-based method developed by Cococcioni and Gironcoli [25] to compute the nonzero second derivative of energy concerning the local occupancy of the metal ion, in which U is given by [40]

$$U \approx \left(\frac{\partial n_I^{\mathrm{scf}}}{\partial V_I}\right)^{-1} - \left(\frac{\partial n_I^{\mathrm{nscf}}}{\partial V_I}\right)^{-1}, \tag{1}$$

where $\partial n_I/\partial V_I$ is the occupation response at the site I, and V_I is the orbital energy shift in the I site. The first and second terms are the self-consistent (scf) and non-self-consistent (nscf) solutions. We consider a

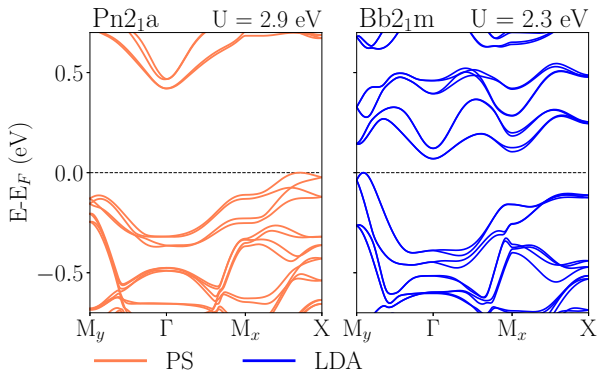

FIG. 6. Band structure using U computed through the linear response method: PS with $Pn2_1a$ structure for $U_{PS} = 2.9$ eV (left) and LDA with $Bb2_1m$ phase using $U_{LDA} = 2.3$ eV (right).

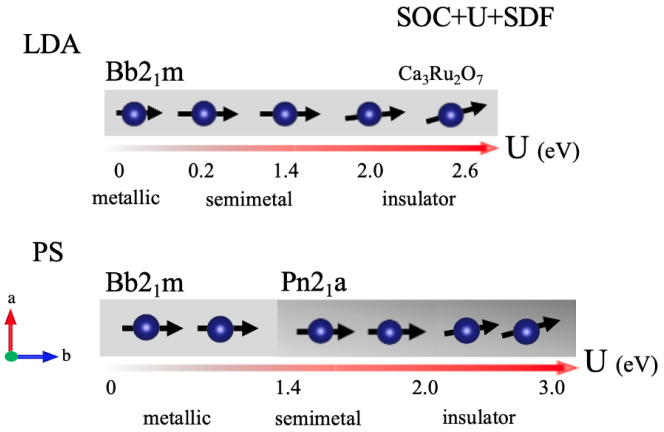

FIG. 7. A schematic representation with the electronic and structural phase transitions as a function of Coulomb repulsion (U) in the presence of spin-orbit coupling (SOC) and structural degrees of freedom (SDF). The black arrows symbolize the spin direction of the Ru atoms (blue balls). As U increases, we can distinguish two main regions: among $0 < U \leqslant 2$ eV in which the spins are along b direction (AFM-b), and for $U > 2$ eV, the spins turn aligned through (111) direction, in which the magnetic moment along b direction is bigger than in the a-c direction ($m_b \gg m_{a,c}$).

perturbation V in the ± 0.2 eV range. As a result of these calculations we found that $U_{PS} = 2.9$ eV and $U_{LDA} = 2.3$ eV for PS and LDA respectively. We have also performed calculations in a lower range of perturbation (± 0.1, with steps $\pm$ 0.02). Here, we detected no large modification of the U value of U_{LDA}= 2.86 eV and U_{ps}= 2.73 eV.

The electronic band structure for the Hubbard U values found by the linear response method is shown in Fig. 6. On the left panel, the PS band structure with $U_{PS} = 2.9$ eV; on the right panel, the LDA band structure with $U_{LDA} = 2.3$ eV. As a result of our calculation, we find that LDA retains the same $Bb2_1m$ symmetry, and the PS approximation keeps the $Pn2_1a$ phase. In the PS approximation, the larger U term value ($U_{PS} = 2.9$ eV) results in a band gap of 0.80 eV at M_x (see Fig. 6, left panel). The large U influence in $Pn2_1a$ structure induces t_{2g} band distribution mainly at M_x, in which the band structure changes from the hybridized bands d_{xz}-d_{yz} for $U = 2.0$ eV to be composed mainly of d_{xz} orbitals (below Fermi level) for $U = 2.9$ eV (see Ref. [36], Fig. S6).

In the case of LDA approximation, the system presents a $Bb2_1m$ symmetry; however, we observe that to increase to $U = 2.3$ eV, the Dirac-like bands are suppressed, emerging a gap of 0.10 eV at M_x similar to the findings from PS approximation at $U = 2.0$ eV (see Fig. 4). The observed gap emerges due to the re-arrangement of t_{2g} orbitals around M_x, as under the PS approximation case. Furthermore, in $Bb2_1m$ structure the large U causes a decrease of the d_{yz} orbital population (see Ref. [36], Fig. S5) and for $U = 2.3$ eV the band occupation of d_{xy}-d_{xz} around M_x below the Fermi level is favored. Additionally, for larger values of the Hubbard U term ($U > 2$ eV), the magnetic state along the b direction becomes unstable, and the magnetic moment direction moves toward the (111) direction in which $m_b > m_{a,c}$. Figure 7 shows a schematic representation of the electronic and structural phase transitions as U increases to 2.6 and 3.0 eV for LDA and PS approximations.

Giving that the structure of the ground state depends on the functional used (PS or LDA), a direct comparison between band structures is meaningless. To compare the band structure for a particular value of the Hubbard U, we set the atomic position and lattice vectors to the $Bb2_1m$ structure (with the atomic position given by the experiment [20] at 8 K). Here, we noticed that regardless of the functional, the gap at M_x appears for $U = 2.3$ eV; however, the system continues metallic (see Ref. [36], Fig. S9). For LDA approximation, the narrow bandgap insulator state appears for U above 2.3 eV (see Ref. [36], Fig. S9 at $U = 2.6$ eV). However, under PS approximation, the band structure favors the metallic character (see Ref. [36], Fig. S9). The metallic behavior tendency could be related to a topological band arising as the U term increases.

We should point out that the narrow band-gap insulator character originates in the strength of U-term independent of the functional choice and structural phase (in the presence of structural degrees of freedom). The $Pn2_1a$ structure favors the insulator state for U $\geqslant$ 2.0 and $\geqslant$ 1.8 eV for PS and LDA approximations, respectively (see Fig. 5), whereas the $Bb2_1m$ favors the insulator character for large U term value, as we can observe for $U = 2.3$ eV Figs. 6 and S5 under LDA approximation.

The large difference in the U term computed through the linear approximation with the values chosen a priory could be related to the DFT self-interaction errors or d-ligand interactions between Ru and O atoms. To develop a Hubbard U correction for the CRO system, it could be necessary to evaluate d interactions for first principles, then construct a Hamiltonian that explicitly contains the d orbitals and the p orbitals of the system as interacting degrees of freedom; however, to solve this in practice could be a tremendous open challenge [39,41].

To enclose our last finding, we suggest that the optimum values of CRO lie among $0.2 \leqslant U \leqslant 2.0$ eV (under LDA approximation); in this range, the band structure agrees with the experimental report. However, for $U \geqslant 1.4$ eV, the band dispersion is strongly pushed to lower energies around the Γ point. The established range of U are in agreement with the U implemented to modulate the electronic structure in

several ruthenium families such as: Ca_2RuO_4 ($1.0 \leqslant U \leqslant 1.5$) [42], Sr_2RuO_4 ($U = 1.5$ eV) [43], and $CaRuO_3$ ($1.0 < U < 2.5$ eV) [44] in which both electronic and structural properties depend of the chosen U value.

V. FINAL REMARKS

We have demonstrated the strong interplay among magnetism, SOC, Hubbard U, and structural degrees of freedom on the electronic properties of CRO. This was done under the density functional theory approach considering two functional choices: LDA and PS approximations.

Depending of the description used, we find contradictory results. On the one hand, the LDA approximation fails to reproduce the correct magnetic ground state of CRO, predicting the AFM-a solution as the most stable AFM configuration; however, the LDA + U approximation for $U \geqslant 0.2$ eV results in the AFM-b alignment as the ground state solution. On the other hand, PS and PS + U approximations successfully describe the AFM-b magnetic configuration as the ground state.

Both LDA + U ($0.2 \leqslant U \leqslant 2.0$) and PS + U ($0.5 \leqslant U \leqslant 1.6$ eV) approximation successfully describe the electronic structure of CRO. However, regarding the structural properties, LDA predicts $Bb2_1m$ phase as the ground state, and PS predicts a structural transition from $Bb2_1m$ to $Pn2_1$a ($U \geqslant 1.4$ eV) [28], being this last one not observed by experiment so far. This new structural transition gives interesting explanations for describing several experimental findings, as explained in Sec. IV 4. However, new experiments will be necessary to support the $Pn2_1$a structure obtained using PS + U approximation.

We conclude that the exchange and correlation functional affects the band occupation mainly at Γ point. On the one hand, the band crosses the Fermi level for PS approximation. On the other hand, a band gap appears for the LDA approximation. Additionally, the primary effect of the Coulomb repulsion (expressed as U term) is to modify the band occupation around the Fermi level with the following main characteristics associated with the exchange-correlation approximation:

PS + U. It is possible to distinguish three regions as the Hubbard U term increases. The system exhibits a metallic character for $U < 1.4$ eV, characterized by a band crossing the Fermi level at Γ and Dirac-like bands at M_x. For $U \geqslant 1.4$ eV, the Bb_1m phase became unstable, and the system relaxes spontaneously into $Pn2_1$a structure, exhibiting a semimetallic state (gap around Γ point) [28], independent of the structural degrees of freedom considered. Finally, for $U \geqslant 2.0$ eV, a semimetal to a narrow band-gap insulator phase transition emerges by opening a gap of 0.16 eV at M_x ($U = 2.0$ eV).

The observed structural transition is independent of the U approach. Along Liechtenstein approach, we find that the transition emerges for $U > 2.0$ eV together with an electronic transition from semimetal to narrow-insulator state (in agreement with PS approximation for $U \geqslant 2.0$ eV).

LDA + U. The $Bb2_1m$ phase is the most stable configuration, and the band structure presents a semimetallic character. For $0.2 \leqslant U \leqslant 2.0$ eV, we evinced a gap around Γ (gap size of 96 meV at Γ for $U = 0.5$ eV) and Dirac-like bands at M_x in good agreement with the band structure reported by the experiments. However, above $U \geqslant 1.4$ eV, the band around Γ is pushed down to lower energies increasing the gap size (as it also happens with PS).

We remark that a narrow band-gap insulator state emerges independent of the functional choice. In the case of PS + U, this happens for $U \geqslant 2.0$ eV (Dudarev scheme) and $U > 2.0$ eV (Liechtenstein approach). For LDA + U, it occurs for $U > 2.0$ eV (Dudarev scheme). Additionally, for these large U values, the magnetic moment along the b direction became unstable, and m goes from [010] to [111] direction in which $m_b > m_{a,c}$.

From these findings, we can give the keys to model the electronic structure of CRO system, establishing the effect of Coulomb repulsion and structural degrees of freedom for two different functional natures. Here, we have shown that CRO is very sensitive to these parameters, in which, as a function of U, it is possible to get a metal, semimetal, and narrow bandgap insulator state independent of the structural degrees of freedom. Depending on the functional choice, the $Bb2_1m$ phase can be stable (LDA) or unstable (PS) in the presence of Coulomb repulsion, SOC and structural degrees of freedom.

The Hubbard repulsion term is usually considered a free parameter, adjusted to improve agreement between calculated and measured properties. This is one of the simplest approaches used to improve the description of the ground state of the many correlated systems, based on the correction of $E_{\mathrm{LDA/GGA}}$ energies, leading to the called "double-counting term (E_{dc})" that models the contribution of correlated electrons to the DFT energy as a mean-field. However, the double-counting term is not uniquely defined, being this an open issue of LDA + U that has been widely discussed; see Ref. [45] for further discussion. Some techniques, such as the linear response approach, can estimate a value for the effective U term. These techniques, however, require further validation. Methods beyond DFT, such as local density approximation + dynamical mean-field approximation (LDA + DMFT), have been successfully used to describe the electronic, structural properties and phase transitions in correlated materials with 4d electrons [45], including Ruddlesden-Popper compounds [46,47]. Studies in this direction could provide a better understanding of CRO, making it possible to compare different description levels on this compound. In this sense, there is still much to explore in CRO systems. In this direction, our study aims to give a first step forward, doing a systematic study of the role of the exchange and correlation in the presence of different degrees of freedom and considering different approximations for the Hubbard U parameter.

While preparing this manuscript, we became aware of a recent experimental report by Hao-Yu *et al* . (Ref. [48]) studying the magnetoresistance and magnetostriction on CRO. This study proposes the use of pulsed magnetic fields to control the magnetic states of CRO. Additionally, in agreement with our results, they reported the stability of magnetic phases (AFM-b, AFM-a) using PBEsol + U with $U = 1.2$ eV. Furthermore, a recent experimental report has studied the CRO under lattice deformation (Ref. [49]), proving that applied strain can be used to tune the spin orientation. These studies confirm the strong correlation between lattice and electronic

degrees of freedom needed to explain the magnetic transitions of CRO.

ACKNOWLEDGMENTS

The authors would like to thank Igor Markovic and Jose Mejía for the fruitful discussions. We thank Fernando Delgado for carefully reading our manuscript and many insightful comments and suggestions. We acknowledge the Max Planck Computing Data Facility for bringing the technical support and Dr. Claudia Felser for providing the VASP license. A.L. thanks to Chilean FONDECYT POSTDOCTORAL Grant No. 3220505 and Danilo Puggioni for aiding with the calculation setup and discussions in the early stage of this project. JWG acknowledges financial support from Chilean FONDECYT: Iniciación en Investigación 2019 Grant No. 11190934 and Chilean FONDECYT Grants No. 1221301 and No. 1220700.

[1] A. Soumyanarayanan, N. Reyren, A. Fert, and C. Panagopoulos, Emergent phenomena induced by spin–orbit coupling at surfaces and interfaces, Nature (London) **539**, 509 (2016).

[2] W. Witczak-Krempa, G. Chen, Y. B. Kim, and L. Balents, Correlated quantum phenomena in the strong spin-orbit regime, Annu. Rev. Condens. Matter Phys. **5**, 57 (2014).

[3] K. Kośmider, J. W. González, and J. Fernández-Rossier, Large spin splitting in the conduction band of transition metal dichalcogenide monolayers, Phys. Rev. B **88**, 245436 (2013).

[4] R. Rejali, D. Coffey, J. Gobeil, J. W. González, F. Delgado, and A. F. Otte, Complete reversal of the atomic unquenched orbital moment by a single electron, npj Quantum Mater. **5**, 60 (2020).

[5] J. W. González, T. Alonso-Lanza, F. Delgado, F. Aguilera-Granja, and A. Ayuela, Complex magnetic orders in small cobalt–benzene molecules, Phys. Chem. Chem. Phys. **19**, 14854 (2017).

[6] G. Cao, S. McCall, J. E. Crow, and R. P. Guertin, Observation of a metallic antiferromagnetic phase and metal to nonmetal transition in $Ca_3Ru_2O_7$, Phys. Rev. Lett. **78**, 1751 (1997).

[7] E. Ohmichi, Y. Yoshida, S. I. Ikeda, N. Shirakawa, and T. Osada, Colossal magnetoresistance accompanying a structural transition in a highly two-dimensional metallic state of $Ca_3Ru_2O_7$, Phys. Rev. B **70**, 104414 (2004).

[8] N. Kikugawa, A. Rost, F. Baumberger, N. J. C. Ingle, M. A. Hossain, W. Meevasana, K. M. Shen, D. H. Lu, A. Damascelli, A. P. Mackenzie *et al.*, $Ca_3Ru_2O_7$: Electronic instability and extremely strong quasiparticle renormalisation, J. Magn. Magn. Mater. **310**, 1027 (2007).

[9] N. Kikugawa, A. Winfried Rost, C. W. Hicks, A. J. Schofield, and A. P. Mackenzie, $Ca_3Ru_2O_7$: density wave formation and quantum oscillations in the Hall resistivity, J. Phys. Soc. Jpn. **79**, 024704 (2010).

[10] G. Cao and L. E. Delong, *Frontiers of 4D-and 5D-transition Metal Oxides* (World Scientific, 2013), Chap. 1.

[11] I. Marković, M. D. Watson, O. J. Clark, F. Mazzola, E. A. Morales, C. A. Hooley, H. Rosner, C. M. Polley, T. Balasubramanian, S. Mukherjee *et al.*, Electronically driven spin-reorientation transition of the correlated polar metal $Ca_3Ru_2O_7$, Proc. Natl. Acad. Sci. USA **117**, 15524 (2020).

[12] H. Xing, L. Wen, C. Shen, J. He, X. Cai, J. Peng, S. Wang, M. Tian, Z.-A. Xu, W. Ku *et al.*, Existence of electron and hole pockets and partial gap opening in the correlated semimetal $Ca_3Ru_2O_7$, Phys. Rev. B **97**, 041113(R) (2018).

[13] M. Horio, Q. Wang, V. Granata, K. P. Kramer, Y. Sassa, S. Johr, D. Sutter, A. Bold, L. Das, Y. Xu *et al.*, Electronic reconstruction forming a C_2-symmetric dirac semimetal in $Ca_3Ru_2O_7$, npj Quantum Mater. **6**, 29 (2021).

[14] D. A. Sokolov, N. Kikugawa, T. Helm, H. Borrmann, U. Burkhardt, R. Cubitt, J. S. White, E. Ressouche, M. Bleuel, K. Kummer *et al.*, Metamagnetic texture in a polar antiferromagnet, Nat. Phys. **15**, 671 (2019).

[15] S. Lei, M. Gu, D. Puggioni, G. Stone, J. Peng, J. Ge, Y. Wang, B. Wang, Y. Yuan, K. Wang *et al.*, Observation of quasi-two-dimensional polar domains and ferroelastic switching in a metal, $Ca_3Ru_2O_7$, Nano Lett. **18**, 3088 (2018).

[16] H. Zhao, H. Zheng, J. Terzic, W. Song, Y. Ni, Y. Zhang, P. Schlottmann, and G. Cao, Lattice flexibility in $Ca_3Ru_2O_7$: Control of electrical transport via anisotropic magnetostriction, Phys. Rev. B **104**, L121119 (2021).

[17] D. Halwidl, W. Mayr-Schmolzer, D. Fobes, J. Peng, Z. Mao, M. Schmid, F. Mittendorfer, J. Redinger, and U. Diebold, Ordered hydroxyls on $Ca_3Ru_2O_7$ (001), Nat. Commun. **8**, 23 (2017).

[18] E. M. J. Johansson, M. Odelius, S. Plogmaker, M. Gorgoi, S. Svensson, H. Siegbahn, and H. Rensmo, Spin- orbit coupling and metal- ligand interactions in Fe (II), Ru (II), and Os (II) complexes, J. Phys. Chem. C **114**, 10314 (2010).

[19] M. Srnec, J. Chalupský, M. Fojta, L. Zendlová, L. Havran, M. Hocek, M. Kyvala, and L. Rulísek, Effect of spin-orbit coupling on reduction potentials of octahedral ruthenium (II/III) and osmium (II/III) complexes, J. Am. Chem. Soc. **130**, 10947 (2008).

[20] Y. Yoshida, S.-I. Ikeda, H. Matsuhata, N. Shirakawa, C. H. Lee, and S. Katano, Crystal and magnetic structure of $Ca_3Ru_2O_7$, Phys. Rev. B **72**, 054412 (2005).

[21] F. Baumberger, NJC Ingle, N. Kikugawa, M. A. Hossain, W. Meevasana, R. S. Perry, K. M. Shen, D. H. Lu, A. Damascelli, A. Rost *et al.*, Nested fermi surface and electronic instability in $Ca_3Ru_2O_7$, Phys. Rev. Lett. **96**, 107601 (2006).

[22] J. S. Lee, S. J. Moon, B. J. Yang, J. Yu, U. Schade, Y. Yoshida, S.-I. Ikeda, and T. W. Noh, Pseudogap dependence of the optical conductivity spectra of $Ca_3Ru_2O_7$: A possible contribution of the orbital flip excitation, Phys. Rev. Lett. **98**, 097403 (2007).

[23] G. Cao, L. Balicas, Y. Xin, J. E. Crow, and C. S. Nelson, Quantum oscillations, colossal magnetoresistance, and the magnetoelastic interaction in bilayered $Ca_3Ru_2O_7$, Phys. Rev. B **67**, 184405 (2003).

[24] J. F. Karpus, C. S. Snow, R. Gupta, H. Barath, S. L. Cooper, and G. Cao, Spectroscopic study of the field-and pressure-induced phases of the bilayered ruthenate $Ca_3Ru_2O_7$, Phys. Rev. B **73**, 134407 (2006).

[25] M. Cococcioni and S. De Gironcoli, Linear response approach to the calculation of the effective interaction parameters in the LDA+U method, Phys. Rev. B **71**, 035105 (2005).

[26] D. J. Singh and S. Auluck, Electronic structure and bulk spin-valve behavior in $Ca_3Ru_2O_7$, Phys. Rev. Lett. **96**, 097203 (2006).

[27] G.-Q. Liu, Mott transition and magnetic anisotropy in $Ca_3Ru_2O_7$, Phys. Rev. B **84**, 235137 (2011).

[28] D. Puggioni, M. Horio, J. Chang, and J. M. Rondinelli, Cooperative interactions govern the fermiology of the polar metal $Ca_3Ru_2O_7$, Phys. Rev. Res. **2**, 023141 (2020).

[29] G. Kresse and J. Furthmüller, Efficiency of *ab initio* total energy calculations for metals and semiconductors using a plane wave basis set, Comput. Mater. Sci. **6**, 15 (1996).

[30] J. P. Perdew, A. Ruzsinszky, G. I. Csonka, O. A. Vydrov, G. E. Scuseria, L. A. Constantin, X. Zhou, and K. Burke, Restoring the density-gradient expansion for exchange in solids and surfaces, Phys. Rev. Lett. **100**, 136406 (2008).

[31] D. M. Ceperley and B. J. Alder, Ground state of the electron gas by a stochastic method, Phys. Rev. Lett. **45**, 566 (1980).

[32] G. M. D. Nguimdo and D. P. Joubert, A density functional (PBE, PBEsol, HSE06) study of the structural, electronic and optical properties of the ternary compounds $AgAlX_2$ (X = S, Se, Te), Eur. Phys. J. B **88**, 113 (2015).

[33] S. L. Dudarev, G. A. Botton, S. Y. Savrasov, C. J. Humphreys, and A. P. Sutton, Electron-energy-loss spectra and the structural stability of nickel oxide: An LSDA + U study, Phys. Rev. B **57**, 1505 (1998).

[34] A. I. Liechtenstein, V. I. Anisimov, and J. Zaanen, Density-functional theory and strong interactions: Orbital ordering in Mott-hubbard insulators, Phys. Rev. B **52**, R5467 (1995).

[35] I. Markovic, Interplay of Spin-Orbit Coupling and Crystal Symmetries in the Electronic Structures of NbGeSb and $Ca_3Ru_2O_7$, PhD. thesis, University of St Andrews, 2020.

[36] See Supplemental Material at http://link.aps.org/supplemental/10.1103/PhysRevMaterials.8.024411 for Secs. SI and SII, which show the structural and electronic properties of CRO, considering spin-orbit interaction, different Hubbard-U parameters, magnetic states, and with and without structural degrees of freedom in all the cases. Section SIII compares the main electronic and structural properties of CRO, considering two approximations to include Hubbard-U repulsion: Dudarev and Liechtenstein.

[37] J. K. Desmarais, J.-P. Flament, and A. Erba, Spin-orbit coupling from a two-component self-consistent approach. II. non-collinear density functional theories, J. Chem. Phys. **151**, 074108 (2019).

[38] J. S. Lim, D. Saldana-Greco, and A. M. Rappe, Improved pseudopotential transferability for magnetic and electronic properties of binary manganese oxides from DFT + U + J calculations, Phys. Rev. B **94**, 165151 (2016).

[39] K. Yu and E. A. Carter, Communication: Comparing *ab initio* methods of obtaining effective U parameters for closed-shell materials, J. Chem. Phys. **140**, 121105 (2014).

[40] Calculate *U* for LSDA+U, https://www.vasp.at/wiki/index.php/Calculate_U_for_LSDA+U.

[41] O. Y. Long, G. S. Gautam, and E. A. Carter, Evaluating optimal U for 3d transition-metal oxides within the SCAN+U framework, Phys. Rev. Mater. **4**, 045401 (2020).

[42] H. D. J. Keen, S. R. Julian, and A. Hermann, *Ab initio* study of pressure-induced structural and electronic phase transitions in Ca_2RuO_4, Phys. Rev. B **104**, 085143 (2021).

[43] H. Iwasawa, Y. Yoshida, I. Hase, S. Koikegami, H. Hayashi, J. Jiang, K. Shimada, H. Namatame, M. Taniguchi, and Y. Aiura, Interplay among coulomb interaction, spin-orbit interaction, and multiple electron-boson interactions in Sr_2RuO_4, Phys. Rev. Lett. **105**, 226406 (2010).

[44] G. H. Zhong, Y. L. Li, Z. Liu, and H. Q. Lin, 4*d* electronic and magnetic characteristics in postperovskite $CaRuO_3$, J. Appl. Phys. **107**, 09E102 (2010).

[45] A. Östlin, W. H. Appelt, I. Di Marco, W. Sun, M. Radonjić, M. Sekania, L. Vitos, O. Tjernberg, and L. Chioncel, Electronic structure of palladium in the presence of many-body effects, Phys. Rev. B **93**, 155152 (2016).

[46] C. Dietl, S. K. Sinha, G. Christiani, Y. Khaydukov, T. Keller, D. Putzky, S. Ibrahimkutty, P. Wochner, G. Logvenov, P. A. van Aken *et al.*, Tailoring the electronic properties of Ca_2RuO_4 via epitaxial strain, Appl. Phys. Lett. **112**, 031902 (2018).

[47] S. Riccò, M. Kim, A. Tamai, S. McKeown Walker, F. Y. Bruno, I. Cucchi, E. Cappelli, C. Besnard, T. K. Kim, P. Dudin *et al.*, In situ strain tuning of the metal-insulator-transition of Ca_2RuO_4 in angle-resolved photoemission experiments, Nat. Commun. **9**, 4535 (2018).

[48] H.-Y. Niu, X. He, Z. Zeng, Y.-J. Song, D.-Q. Jiang, H. Huang, Y.-Y. Liang, L.-X. Xiao, Z.-W. Ouyang, and Z.-C. Xia, Magnetoresistance relaxation steps originating from dynamic spin-orbital interactions in $Ca_3Ru_2O_7$, Phys. Rev. B **106**, 174415 (2022).

[49] C. D. Dashwood, A. Walker, M. P. Kwasigroch, LSI Veiga, Q. Faure, J. G. Vale, D. G. Porter, P. Manuel, D. D. Khalyavin, F. Orlandi *et al.*, Strain control of a bandwidth-driven spin reorientation in $Ca_3Ru_2O_7$, Nat. Commun. **14**, 6197 (2023).